Analysis of Flow Cytometry DNA Damage Response Protein Activation Kinetics Following X-rays and High Energy Iron Nuclei Exposure

Lori J. Chappell[1], Mary K. Whalen[2], Sheena Gurai[2], Artem Ponomarev[1], Francis A. Cucinotta[3] and Janice M. Pluth[2,]*
[1]U.S.R.A., Division of Space Life Science Division
Houston, TX 77058, USA

[2]Lawrence Berkeley National Laboratory, Life Sciences Division,
One Cyclotron Road, Berkeley, CA 94720, USA

[3]NASA, Lyndon B. Johnson Space Center, 2101 NASA Parkway, Houston TX 77058, USA

*****Corresponding author
Janice M. Pluth
Phone: (510) 486-5799
Fax: 510-486-6816
E-mail: JMPluth@lbl.gov

33 Pages of text including references
3 Tables
7 Figures (4 color)
2 Pages of figure legends

KEYWORDS: Space radiobiology, ATM, γH2AX, ATF2, high LET, signal transduction

Running title: Analysis of Flow Cytometry DNA Damage Activation Data

Chappell, L.J., Whalen, M.K., Gurai, S., Ponomarev, A., Cucinotta, F.A. and Pluth, J.M. Analysis of Flow Cytometry DNA Damage Response Protein Activation Kinetics Following X rays and High Energy Fe Nuclei Exposure. ***Radiat. Res.***

We developed a mathematical method to analyze flow cytometry data to describe the kinetics of γH2AX and pATF2 phosphorylations ensuing various qualities of low dose radiation in normal human fibroblast cells. Previously reported flow cytometry kinetic results for these DSB repair phospho-proteins revealed that distributions of intensity were highly skewed, severely limiting the detection of differences in the very low dose range. Distributional analysis reveals significant differences between control and low dose samples when distributions are compared using the Kolmogorov-Smirnov test. Radiation quality differences are found in the distribution shapes and when a non-linear model is used to relate dose and time to the decay of the mean ratio of phospho-protein intensities of irradiated samples to controls. We analyzed cell cycle phase and radiation quality dependent characteristic repair times and residual phospho-protein levels with these methods. Characteristic repair times for γH2AX were higher following Fe nuclei as compared to X-rays in G1 cells (4.5±0.46 h vs 3.26±0.76 h, respectively), and in S/G2 cells (5.51±2.94 h vs 2.87±0.45 h, respectively). The RBE in G1 cells for Fe nuclei relative to X-rays for γH2AX was 2.05±0.61 and 5.02±3.47, at 2 h and 24-h post-irradiation, respectively. For pATF2, a saturation effect is observed with reduced expression at high doses, especially for Fe nuclei, with much slower characteristic repair times (>7 h) compared to X-rays. RBEs for pATF2 were 0.66±0.13 and 1.66±0.46 at 2 h and 24 h, respectively. Significant differences in γH2AX and pATF2 levels comparing

irradiated samples to control were noted even at the lowest dose analyzed (0.05 Gy) using these methods of analysis. These results reveal that mathematical models can be applied to flow cytometry data to uncover important and subtle differences following exposure to various qualities of low dose radiation.

INTRODUCTION

An improvement in the understanding of the potential health risks from space radiation is needed to support space exploration by human beings. Space radiation and terrestrial low dose exposures (*1-3*) occur at low dose-rates where in some cases only a single radiation track interacts with a small population of cells over many hours to days. The high charge and energy (HZE) ions in space produce distinct distributions of DNA and oxidative damage in cells (*2-5*) compared to terrestrial forms of radiation, thus complicating approaches to risk estimation due to the lack of human data for effects from these types of radiation exposures. Energy deposition from HZE nuclei is heterogeneous exhibiting both high and low LET characteristics from direct traversal of cells and from the secondary electrons ejected, called δ-rays. In order to understand space radiation risks, experimental techniques to study low dose exposures in individual cells are warranted. The visualization of repair foci using immunohistochemistry and microscopy is a commonly used single cell assay to look at DNA repair response following radiation exposure. A less commonly used single cell assay that can be used to detect cellular response to radiation is flow cytometry, which allows the rapid analysis of a large number of cells (>10,000). In this report we describe mathematical methods to statistically analyze flow cytometry data for phospho-proteins activated in mammalian cells following irradiation in order to improve the understanding of the low dose response.

Flow cytometry can be used to measure the intensity of fluorescently tagged bio-molecules within individual cells (*8,9*). We have developed flow-based assays to measure

phospho-protein levels of proteins known to be important in responding to ionizing radiation exposure (*10*). By dually staining cells with propidium-iodine (PI), which labels total DNA content, and a fluorescently-labeled antibody conjugated to a DNA damage response phospho-protein (γH2AX or pATF2 $Ser^{490/498}$), we were able to determine both the cell cycle phase and the level of specific phospho-proteins in individual cells within a population. Samples were fixed various times after exposure to various doses of high and low LET radiation, providing a very comprehensive data set from which to study how radiation quality affects phospho-kinetics. Because of the highly skewed nature of the median and variances reported in our earlier work (*10*) we have gone on to study the data on an individual cell basis, to enable detection of differences following very low doses. Here we show that this more complex analysis provides a more rigorous approach to study radiation effects in the low dose range.

DNA double strand breaks (DSB) induced by different radiation qualities lead to specific dose dependent signaling processes affecting cell death, mutation, differentiation, pre-mature senescence and genomic instability (*11-14*). Early responding signal transduction proteins following irradiation include MRN, 53BP1, ATM, and DNA-PK_{cs}. The activation step of DNA-PK_{cs} and ATM is rapid occurring from 3 to 30-minutes following irradiation (*15,16*). Both activated proteins have been shown to lead to the phosphorylation of the histone variant H2AX in a chromatin region corresponding to about 2-Mbp around the DSB, with the phosphorylated form denoted γH2AX (*17,18*). Total numbers of γH2AX foci have been shown to be fairly representative of the total number of DSBs (*19,20*). However, the kinetics of induction and dephosphorylation, and

the background levels of γH2AX vary throughout the cell cycle, making it difficult to unambiguously equate the number of γH2AX foci to the number of DSBs.

Besides γH2AX, ATM activates many downstream kinases including pATF2 and pSMC1, two phospho-proteins studied in our earlier report (*10*). Activating Transcription Factor 2 (ATF2) was originally identified as a transcription factor regulated by JNK/p38 and involved in cellular response to stress (*21*,*22*). More recently it has been shown to have a role in DSB repair, which is independent of its transcriptional roles (*23*). ATM has been shown to phosphorylate ATF2 on Serines 490 and 498 following ionizing radiation (*23*). Phosphorylated ATF2 foci have also been shown to co-localize with γH2AX and Mre11/Rad50/NBS1 foci (*24*,*25*). Inhibition of ATF2 results in a decreased recruitment of Mre11 to ionizing radiation induced foci (IRIF), abrogates the S phase checkpoint, reduces activation of ATM, Chk1 and Chk2, and increases a cells radio-sensitivity (*25*). SMC1 is phosphorylated on serine 957 by ATM in response to DSBs in an NBS-dependent manner and co-localizes with γH2AX and other proteins at the site of DSBs (*24*,*25*). SMC1 has diverse roles in chromosome segregation and NHEJ vs HR choice (*25*,*26*). Our previous work (*8*) revealed pATF2 and pSMC1 induction by Fe nuclei was reduced compared to γH2AX, with more similar induction of all three of these phospho-proteins being observed following X-rays.

We developed a mathematical approach to analyze FACS data detailing cell-cycle dependent distributions of phospho-proteins important in the DNA damage response. Of interest are methods to test the significance of results at low doses (0.1 Gy or less) and to identify both qualitative and qualitative differences in phospho-protein distributions produced by low and high LET radiation. A scatter plot of γH2AX intensity following 0.5

Gy Fe nuclei, with control cells shown in blue and irradiated cells in red, illustrates the objective of the mathematical analysis (Fig.1). Techniques would be useful to sort data by cell cycle and distinguish intensity levels found in control cells from the additional intensity induced by radiation. The primary goal of this work is to identify the underlying distributions produced by radiation and to use the resulting information to make quantitative descriptions of dose, time, and radiation quality differences for each cell phase and distinct phospho-protein.

METHODS AND MATERIALS

Experimental Methods

Cellular experimental methods are the same as reported recently by Whalen et al (*10*) and are briefly summarized below.

Cell Culture

82-6 hTERT immortalized fibroblast cells (courtesy of Judith Campisi) were grown in DMEM medium (all medium and supplements from Gibco, Invitrogen, Carlsbad, CA) supplemented with 10% fetal bovine serum, antibiotic-antimycotic (1X) and l-Glutamine (2mM). T75 flasks were set up for each time point and dose, and grown to 85 to 95% confluence prior to exposure. Approximately 80% (+/-10%) of the cells were in G1 at the time of radiation for all experiments.

Irradiation Conditions

Cells were exposed to 4 doses (0.05, 0.1, 0.5 and 2 Gy) of 320 kV X-ray or 1000 MeV/u Fe nuclei (LET of 150 keV/μm). X-ray exposures were performed at Lawrence Berkeley National Lab, using dose rates ranging from 0.05 Gy/min to 0.8 Gy/min depending on dose. Fe nuclei exposures were performed at Brookhaven National Lab using dose rates ranging from 0.1 to 1 Gy/min depending on dose. Three independent experiments for both Fe and X-ray data were performed.

Antibodies

Primary antibodies used included mouse monoclonal γH2AX (1:800 dilution) from Upstate (Lake Placid, NY), and rabbit polyclonal pATF2 $Ser^{490/498}$ (1:1000 dilution) from PhosphoSolutions (Aurora, CA). Goat anti-mouse 488, and goat anti-rabbit 488 secondary antibodies from Molecular Probes (Invitrogen Carlsbad, CA) were used with the appropriate primary antibodies. Cell cycle status was determined by staining cellular DNA with propidium iodide (PI, Roche Applied Science, Indianapolis, IN), and used at a final concentration of 10 μg/ml. RNase A purchased from Sigma-Aldrich (St. Louis, MO) was used at a final concentration of 100 μg/ml.

Fixation and staining for Flow cytometry analysis

Flasks were fixed at various time points (0.5, 2, 4, 8 and 24 h) post irradiation, and a control was fixed at each of these time points as well. A methanol fixation was optimized for γH2AX, and cells were fixed with paraformaldehyde followed by a subsequent methanol fixation for optimal staining of pATF2 $Ser^{490/498}$. After fixation cells were placed at -20° C until they were stained. Cell suspensions were counted prior to

staining and set up at 1.0 x 10^6 /ml. An aliquot of the fixed cells containing 0.5 to 1.0 x 10^6 of cells was removed and washed in PBS for each staining. Cells were placed in a blocking solution containing 2% FBS/PBS and incubated for 1 h with primary antibody on ice. Following incubation, cells were pelleted and washed in PBS, then incubated in a secondary antibody diluted (1:400) in blocking solution. After 1 h additional incubation on ice under foil, cells were pelleted and washed for a final time in PBS. Cells were then resuspended in PBS containing PI and RNase A, or in RNase A alone to ensure that the addition of PI did not affect the 488 spectra. Samples were analyzed on Becton-Dickinson FACS Calibur flow cytometry machine, and at least 10,000 events were collected per sample. Fluorescence values for γH2AX labeled with Molecular Probes 488 secondary antibody were captured in the FL1 channel in log scale, and PI signals were captured in the FL3 channel using linear scale. The main cell population of cells was centered in FSC vs. SSC gate. Cell doublets were eliminated prior to analysis, and values for each cell were exported using Flowjo software (TreeStar Inc., Ashland, OR.) and analyzed as described below.

Mathematical Analysis

We developed mathematical methods to analyze the distribution of the phospho-proteins: γH2AX and pATF2 in each phase of the cell cycle. Raw data from flow cytometry experiments was exported using FlowJo software (TreeStar Inc., Ashland, OR.) and resulting experimental data sets placed into extensive data files for analysis. DNA cell cycle phase was determined by the propidium iodide (PI) signal intensity in cells stained with PI, as signal is proportional to the amount of DNA present in cells when stained

with this DNA intercalating agent. We assumed normal cell cycle distributions of cells in G1/G0 phase and that cells in G2/M phase would be symmetrical about their respective modes, and Gaussian. Our analysis approach was to first identify G1 and G2/M phase cells represented by Gaussian distributions with the peak intensity of these distributions expected to be two-fold apart based on their DNA content. Early and late G1 populations were also identified, populations which would be expected from our biological understanding of G1 phase.

To represent the broader S-phase distributions common approaches are to use a single or double Gaussian model or a trapezoidal distribution, although other functional forms could also be considered in analysis. However, the irradiated cells under consideration were largely confluent, with approximately 80% of the cells in G1 phase. Because S phase cells contributed little to the data sets we were not able to distinguish different types of S-phase distributions (single or double Gaussian, trapezoidal or non-parametric distribution after G1 and G2/S subtraction) in our data analysis. It is likely that for other data sets including cells in exponential growth or synchronized cells a larger S-phase contribution would occur and we could then test different S-phase forms. As discussed by Eudey (*28*), the assumptions about the shape of the S-phase distribution are less rigid in the literature. Our assumptions about S-phase follow those proposed by Fried (*27*), who used a series of broadened Gaussian curves to fit the S-phase distribution (*28*). Assuming that all cell cycle phases follow distinct Gaussian distributions, model based clustering and normal mixture modeling was utilized to identify a Gaussian distribution for each phase. The MCLUST software (*29*) was used to identify the cell cycle phase distributions as a function of the PI value. Separate clustering analysis was

performed for each individual replicate experiment. Cell cycle population results obtained were checked using FlowJo software and found to be in good agreement.

The clustering software was able to identify cells in early G1, late G1, early S, late S, and G2/M as separate Gaussian distributions. For a given PI value the probability of a cell being in a specific phase was assigned based on the Gaussian distributions dependence on PI. Once the phase was identified for each cell, further analysis was performed to compare the control samples' phospho-protein intensities to the irradiated samples' phospho-protein intensities.

We analyzed differential and cumulative distributions of phospho-protein intensities for each radiation quality, dose, time after irradiation, and cell cycle phase. We used kernel density estimates with a Gaussian kernel function to create a smoothed, empirical approximation for the density (distribution of intensity per cell) of γH2AX and pATF2. We tested if the levels of the various phospho-proteins were increased in the irradiated samples at various times post-irradiation compared to their matched control samples using the Kolmogorov-Smirnov test statistic (*30*). Here the cumulative distribution of fluorescence intensity in n_1 controls cells, $F_0\,(FL1)$ and n_2 irradiated cells at dose D, $F_D\,(FL1)$ were formed from single cell data, and the maximum difference between the distributions in the positive direction was considered. The positive statistic corresponding to an increase in the irradiated sample is given by:

$$(1) \quad Z^+ = \max\left[F_0(FL1) - F_D(FL1)\right]$$

The *p*-value for individual experiments were then combined using Fischer's method where χ^2 is given by:

$$(2) \quad \chi^2 = -2\sum_i \ln(p_i)$$

with 6 degrees of freedom for our triplicate samples.

To control for factors such as variability in the control samples, inter-comparison of results for individual experiments from triplicates, and for comparisons between different irradiation types made at different facilities (Fe nuclei at NSRL and X-rays at LBNL), a scaling approach was introduced. We observed that the median level of the control samples was the most reliable indicator of this variability, as the mean was more influenced by the outliers of a small number of cells than the median. The scaling variable which we used for these studies was the fold-increase in the median value phosphorylation level of the irradiated group over the control for each independent staining, denoted as *X*. This allowed for normalization of the data and for comparisons to be made between independent experiments. After determining the median FL1 values of each matched control sample (Median-controls), we defined for any level of fluorescence in the irradiated samples at a specific time, dose and radiation quality the distribution, *P (FL1)*, and the transformed distribution, *P (X)* where *X* is given by:

$$(3) \quad X = \frac{FL1(irradiated - sample)}{FL1(Median - controls)}$$

Comparing Phospho-Protein intensities

The ratio of means (*RoMn*) was calculated for each time and cell cycle phase individually to compare the control samples' phospho-protein intensity to the irradiated samples' phospho-protein intensity as described by Friedrich (*31*). The *RoMn* measures the difference in effect for a continuous outcome similar to a risk ratio or odds ratio for binary effect measures and allows for comparisons across replicates with different intensity strengths. The *RoMn* for each time point and cell cycle phase can be defined as:

$$(4) \qquad RoMn = \frac{mean_{irradiated}}{mean_{control}}.$$

The variance of its natural logarithm was estimated as:

$$(5) \qquad Var\left[\ln\left(RoMn\right)\right] = \frac{1}{n_{irradiated}}\left(\frac{sd_{irradiated}}{mean_{irradiated}}\right)^2 + \frac{1}{n_{control}}\left(\frac{sd_{control}}{mean_{control}}\right)^2$$

and used to create weights for the non-linear decay models relating time and dose with the *RoMn*. In a small number of cases a control sample was not available for a particular time point, and in these cases a weighted average of the control means for all time points available in that experiment was used to estimate $mean_{control}$ for the missing time point.

Repair Kinetics Representation

The loss of γH2AX intensity at longer times post exposure has been correlated with DNA repair. In order to consider the dependence of repair-time on radiation quality and dose, the following non-linear model was considered for the Ratio of Means (*RoMn*):

$$(6) \qquad RoMn = N\exp\left(-t/t_c\right) + C_0$$

Note that the constant, C_0 would have a value of 1 if the phospho-proteins returned to control levels at long times after irradiation. We fit individual models to each X-ray or Fe nuclei replicate separately for each dose and cell phase. The results of the analysis for early G1 and late G1 did not differ significantly. For S and G2/M data, the variability in the *RoM* estimates could not identify a difference between the S phase and the G2/M phase, and therefore these data were merged combining replicates into one model. This

results in six estimates for the *RoM* at each time point and dose corresponding to triplicate experiments for early and late G1 or similarly triplicate experiments for S and G2/M cell phase.

A sensitivity analysis was performed to determine how the individually estimated constants for each dose could be combined into one model. A linear relationship was found between Dose and the constants N and C_0. The new model formulation follows:

$$(7) \qquad RoMn = (Dose \times N_1)\exp\left(-t/t_c\right) + 1 + Dose \times C_1 .$$

The regression model was weighted by the standard error of the *RoMn* estimates. The model estimates were checked for robustness by relaxing the assumptions on independence within replicates and by fitting mixed-effects models. Note that at zero dose the *RoMn* is 1 for all times as expected.

For pATF2 a saturation effect is observed at higher doses. This was modeled by adding an additional term with a dose-squared dependence with strength parameter, N_2 to the model:

$$(8) \qquad RoMn = (Dose \times N_1 + Dose^2 \times N_2)\exp\left(-t/t_c\right) + 1 + Dose \times C_1$$

The RBE for γH2AX and pATF2 at different time points was then evaluated using equations (7) or (8) and the fitted parameters are described below.

RESULTS

Modeling Predicted Numbers of DSBs Following Low and High LET Radiation

Our mathematical approach allows us to assign fractional contributions from each cell phase for radiation or background levels of γH2AX intensity to the scatter diagram. Ionizing radiation produces a stochastic distribution of DSB's in cells, which is distinct for low LET X-rays and high LET heavy ions. A schematic diagram describing the relationship between increasing PI fluorescence, indicative of cell cycle phase, and γH2AX intensity is shown in Figure 1. Background and radiation (0.5 Gy Fe nuclei) induced signals 0.5 h after exposure, are overlaid in blue and red respectively. In order to understand the underlying distribution of intensity and how it may relate to the DSB distribution we describe model dependent estimates of the initial DSB distribution in Figure 2. The predictions for X-rays are based on the Poisson model with a mean of 25 DSB/Gy. The predictions for Fe nuclei are from the model of Ponomarev and Cucinotta (*34*) and use a random walk model of human chromosomes built from 2 kbp monomer segments, constrained into chromosomal territories combined with a track structure code to predict the distribution of DSBs in an individual cell. The mean number of DSB's is very similar for X-rays and Fe nuclei, however Fe nuclei display a larger fraction of cells with no DSBs at low dose and a pronounced skew-ness to high numbers of DSBs/cell at all doses compared to X-rays. Of note is that at the lowest dose of 0.05 Gy, both Fe nuclei and X-rays are predicted to have a proportion of cells with no DSB's.

Differing Phospho-protein Kinetics Dependent on Cell Cycle and Radiation Quality

γH2AX intensity in different phases of the cell cycle 2 h post X-rays (Fig. 3a) and Fe nuclei (Fig. 3b), following exposure to different doses is described using a density distribution and a kernel smoothing approach. The clustering model is able to distinguish

early and late G1, early and late S, and G2-M phases. The smoothing algorithm allows us to represent the data as a continuous distribution denoted as the density of a phospho-protein, and can be contrasted to our previous binning approach (*10*), with the latter sensitive to the number and widths of the bins chosen. The cumulative distribution found by integrating the density, or similarly from ranking cell counts with increasing phospho-protein levels is shown in Fig. 4, and is used in the KS sensitivity test described below. Results for the density distribution for pATF2 at 2 h post X-ray or Fe nuclei irradiation are shown in Fig. 5. Comparison of Fig.'s 3 and 5 suggests that Fe nuclei produced a broader distribution of γH2AX intensity than X-rays, as predicted by the calculations of the frequency of the number of DSB's per cell shown in Fig. 2. However, the comparison also suggests the pATF2 distributions for X-rays and Fe nuclei were more similar in shape although X-rays produced a higher mean intensity as reported previously (*10*). These results suggest that γH2AX is more representative of the initial stochastic distribution of DSBs than pATF2.

To reduce variability across our triplicate experiments we have scaled the intensity of specific phospho-proteins to the median of the control distribution in their matched experiment as described in the Methods section and used this for further comparisons. To further describe the broader distribution of γH2AX for Fe nuclei compared to X-rays; reflective of differences in track structure between radiation types, we evaluated the width of the distribution defined as range of the scaled phospho-protein intensity at the 10% and 90% percentile averaged over replicate experiments. These results reveal that Fe nuclei produce significantly broader distributions than X-rays for γH2AX (Fig. 6). In contrast, pATF2 spectra following X-rays, exhibits a slightly larger

width than following Fe nuclei exposure. This suggests that pATF2 induction is less reflective of the initial damage distribution observed following Fe nuclei exposure.

Modeling and Statistical Analysis of Flow Data

The KS-test reveals that G1 distributions for irradiated samples were significantly increased over the control distribution (p-values $<10^{-20}$) for all doses and times. The p-values for KS-test results for replicate experiments (Eq. 2) of the combined S-G2/M data sets are shown in Table 1 for γH2AX and pATF2. For the higher doses (0.5 and 2 Gy) extremely low p-values were obtained for all timepoints ($<10^{-20}$), and thus we decided to focus the table on low dose results. For γH2AX following X-ray significant differences were primarily noted at the earliest timepoint (0.5 h), prior to repair of damage. Whereas following high LET exposure the earliest timepoint did not reveal a significant difference from controls although all subsequent times did exhibit significant differences, reflective of the complex breaks induced by high LET damage and the residual levels often observed. For pATF2 more similar results were obtained following both radiation qualities with insignificant results observed at the lowest dose and longest time point, again likely indicative of full repair and the cells return to baseline. The variations in p-value below 10^{-3} are not viewed as important, other than revealing that a highly significant result was found for S-G2/M induction of γH2AX and pATF2 over control levels at a given dose or time point. The variability observed is likely reflective of the small fraction of cells in S-G2/M compared to G1 where the majority of the cells resided in these experiments (~80% of the population)(*10*). However our data reveal that our

flow cytometry methods are quite sensitive in detecting differences even with these smaller sample sizes and following very low doses.

Figure 7A shows results for the ratio of the means of γH2AX following 2 Gy of X-ray or Fe nuclei and the resulting fits of the data using Eq. (7). Figure 7B shows results for pATF2 and fits from Eq. (8). Table 2 shows the model decay parameters that resulted from fitting the models of Equations (7) and (8) to FACS data for γH2AX and pATF2. The higher values of C_1 found for Fe nuclei compared to X-rays is an indication of the higher levels of residual damage. Values of N_1 measure the strength of initial damage induction, and are higher for pATF2 induction following X-ray in G1 and S/G2 phase cells, for γH2AX in S/G2 phase cells following X-ray, and in G1 following Fe nuclei exposure. The average repair time, t_{rep} was found to be higher for Fe nuclei for each phospho-protein independent of the phase of the cell cycle. For γH2AX in S/G2 cells the parameter C1 in Table 3 is negative for both Fe nuclei and X-rays indicating that residual levels are about the same albeit Fe nuclei showed slower repair at earlier times. The values of the parameter N_2 that appears in Equation (8) describing the decay curve for pATF2 in Table 2 are negative suggesting that pATF2 induction saturates as dose is increased, which may be predicted from the dose saturation reported previously for pATM (*15*).

DISCUSSION

Flow cytometry has not been used extensively in the study of radiation effects with the exception of its use in determining cell phase distributions. However, because of its ability to rapidly measure signals in a large number of cells ($>10^4$), and sort them by

cell cycle phase, we are pursuing this approach to study the heterogeneity of damage in individual cells especially for the difficult task of understanding responses at low doses of heavy ion exposure. In our previous report (*10*) we noted the highly skewed nature of the distributions of phosphorylation levels for various phospho-proteins. In this report we have described mathematical analysis approaches to treat such distributions. The resulting analysis is able to demonstrate significant differences at low doses, and to unfold large amounts of quantitative data including decay times, RBEs, and single ion response distributions. As noted in computer modeled data of Fe nuclei vs X-ray exposed cells (Fig. 2), distinct differences in the initial distributions of DSBs and thus phospho-patterns would be expected based on the radiation quality of an exposure. The data appear to reflect what we have predicted through modeling, revealing wider γH2AX peaks following Fe nuclei as compared to X-ray (Fig. 3b vs 3a). Further comparisons of biophysical models (*5, 6, 36*) to the experiments will be reported elsewhere.

Foci experiments using immunohistochemistry are now a common approach for observing the DNA damage responses at low dose. Immunohistochemistry can be used to image DNA damage response proteins under a microscope allowing for a spatial description of damage. However, HZE nuclei produce streaks of foci (*35*) which are often not quantifiable; and in most cases only a verification of the number of ions per cell as described by the Poisson distribution, and the cell area can be made. Therefore, the evolution of initial streaks or clusters of foci to individual foci observed at later post-irradiation time can not lead to reliable estimates of repair kinetic parameters for heavy ion induced foci as they pertain to DNA repair using immunohistochemistry.

Experiments with HZE ions must consider the clustering of DNA damage along the path of the ion, which leads to multiple DSB's within small inter-genomic distances (*6, 34*). The impact parameter, defined as the distance from an ions track to the center of a biomolecule, is a stochastic variable resulting in complexity in the initial DSB distribution due to some cells receiving direct ion traversals and other cells only receiving δ-rays. Furthermore, the Poisson distribution of the number of ion hits per cell and the geometry of the DNA within the cell nucleus leads to additional complexity of the DNA damage distribution. At distances of a micron or more from the track, δ-rays will infrequently produce damage foci; however these may be obscured by the unavoidable background of foci observed in experiments, limiting the applicability of foci counting experiments to discern the δ-ray contribution to the overall biological effect of HZE ions. FACS assays, although not providing spatial information other than localization to a single cell nucleus, does allow for rapid detection of a large number of cells (10^4 or more) in a cell cycle phase dependent manner. In contrast, foci counting experiments usually analyze only a few hundred cells and cell cycle information can be difficult to quantify. For both flow cytometry and foci approaches statistical analysis of background levels must be considered to understand responses at low doses or dose-rates.

Our previous studies looking at phospho-protein kinetics based on median fold increases over controls revealed a specific defect in the induction of ATM mediated phosphorylations following high LET when compared to equal dose exposures of low LET. The current study, in which we have more carefully analyzed the response on a single cell level collaborates this major finding. This attenuated response may be critical in that even transient inhibition of ATM function has been shown to result in an increased

radiation sensitivity if it occurs during or closely after irradiation (*37*). Failure to fully activate ATM following high LET exposure may explain the increased sensitivity observed for high LET exposures as compared to X-rays. This study goes further than our previous work in providing analysis tools to detect significant differences even at very low levels of damage.

Recent publications have suggested a lack of correlation between the number of γH2AX foci formed early after IR and radiosensitivity, but the kinetics of disappearance did correlate with survival (*38, 39*). When comparing high vs low LET radiations we see an increase in γH2AX levels as compared to X-ray at early time points as well as a greater level of residual foci at 24 h post irradiation. For pATF2 the initial induction is not as great following high LET however the residual level is greater as compared to low LET. If residual levels do correlate with survival as previous studies have suggested, this again points to a greater efficiency for high LET in promoting negative cellular effects. Previous work as well as our current study has revealed a leveling out in pATF2 induction between 0.5 and 2 Gy for both X-ray and Fe nuclei exposed cells, whereas γH2AX levels show a linear dose-response. Other studies looking at pATM induction following low LET exposure have noted that 50% of the ATM molecules were phosphorylated after a 0.5 Gy dose, implying only 50% of the molecules are available for phosphorylation with even higher doses (*15*). This seems to fit with our results in which we see little difference between pATF2 induction between 0.5 and 2 Gy, although doses under 0.5 Gy appear to show a very linear increase with dose.

An increased radioresistance in late S phase has previously been documented for cells exposed to X-ray (*40-41*). Our data also seem to support this finding as noted when

reviewing representative decay ratios of γH2AX following 2 Gy (Fig. 7A). γH2AX decay ratios plotted in S/G2 come down to baseline levels much sooner than cells in G1 following both X-ray and Fe exposure. However, a greater induction and longer repair time for G1 cells as compared to S/G2 is also noted in these graphs for both radiation qualities. Fe nuclei exposure appears to induce a much lower induction of γH2AX in S phase cells as compared to G1 cells, whereas more equal inductions between these cells cycles are noted following X-ray. More recently it has been reported that unlike X-ray, high LET exposures actually result in an increased radiosensitivity in S phase cells (42). This finding could also be supported by our data when comparing repair times for S/G2 cells following Fe nuclei vs X-ray exposures (5.51$\pm$2.94 h vs 2.87$\pm$0.45 h, respectively). However, decay ratios do not appear to show much of difference between S/G2 phase cells beyond an initial lowered induction following high LET as compared to low LET. It has been hypothesized that the improved radioresistance in S phase noted following X-ray likely results from the process of DNA replication, whereas the decreased radioresistance following high LET may be due to an inability of Ku to bind to the much smaller fragments induced following high LET damage (*40, 42*). Unlike γH2AX kinetics, pATF2 decay plots (Fig.7B) are much more similar between the radiation qualities in S/G2 and differ primarily in their G1 kinetics, with Fe nuclei exposures showing a much lower induction, yet greater residual level of pATF2 as compared to X-ray. The reason for this difference in kinetics based on radiation quality likely has to do with the differing role(s) of pATF2 as compared to γH2AX following damage, including pATF2's importance in cell cycle check point control. Since for these experiments the majority of cells were in G1 at the time of radiation ($\geq$80%) and not designed to best detect effects of

radiation on cells in S and G2, we cannot make definite conclusions from the current results for the smaller percentage of cells in S/G2. Future experiments using purified populations of S and G2 cells isolated by synchronization or cell sorting are planned to better address differences in phospho-protein kinetics in these phases of the cell cycle.

Pulsed-field gel electrophoresis (PFGE) studies, which are made at high doses (10 Gy or higher), have been used to determine RBE's and characteristic DSB rejoining times for X-rays and ions (*43-46*). The differences in track structure due to the number of tracks per cell and doses from δ-rays is a concern when considering the high doses necessary for PFGE experiments to applications at low doses. Only the inner part of a track (core) of single heavy ions intersect small segments of DNA, even at doses as high as 100 Gy due to the small geometric area of a DNA segment. However there are substantially smaller contributions from δ-rays at the low doses used in our experiments compared to the high doses used in PFGE experiments. In contrast the DNA fragment distribution detected by PFGE will likely reflect more than one ion track within a kbp or higher DNA fragment, resulting in two or more cuts, and the variation in δ-ray doses from overlapping tracks will also increase with increasing ion fluence. The RBE values we have determined for γH2AX induction are larger then the RBE estimates for DSBs made using PFGE (*43-46*), which generally showed values less than 2. The low RBE's determined by PFGE have been attributed to an inability to resolve clustered DSBs.

PFGE experiments are often interpreted using fast and slow rejoining components. The fast component has been shown to be influenced by the presence of heat-labile sites (*47*). In contrast, our γH2AX measurements may fail to detect a fast component given our earliest timepoint is ½ h post irradiation when foci levels generally

peak, likely due to the multiple biochemical steps involved in the activation of γH2AX and its dephosphorylation (*36*). However, only high doses of irradiation can be used in PFGE experiments, thus γH2AX measurements are more relevant when trying to determine effects at low doses. Our characteristic times for pATF2 would be distinct from times for the rejoining of DSBs or removal of γH2AX, since they are related to the S-phase cell cycle delay induced by pATM (*21-23*). For both γH2AX and pATF2, flow cytometry can make assessments of cell cycle related parameters as reported here and in our earlier report (*10*), while PFGE can not resolve cells in individual cell cycle phases, and the large doses used involve extensive cell cycle arrests.

In summary, using flow cytometry and mathematical analysis we have been able to show the extreme sensitivity of our methods for uncovering DNA damage responses at low doses (down to 0.05 Gy). These methods can be applied to a broad range of problems of interest in improving our knowledge of the biophysics of low LET and heavy ion effects at doses reflective of occupational exposures on Earth or during spaceflight.

ACKNOWLEDGEMENTS

We gratefully acknowledge partial financial support provided by the NASA Space Radiation Program (03-OBPR-07-0032-0027) and by the Director, Office of Science, Office of Basic Energy Sciences, of the U.S. Department of Energy under Contract No. DE-AC02-05CH11231.

Disclaimer

REFERENCES

1. National Council on Radiation Protection and Measurements, Information needed to make radiation protection recommendations for space missions beyond Low-Earth Orbit. NCRP Report No. 153**,** Bethesda, MD (2006).

2. F.A. Cucinotta and M. Durante, Cancer risk from exposure to galactic cosmic rays: implications for space exploration by human beings. *Lancet Onc.* **7**, 431-435 (2006).

3. M. Durante, and F.A. Cucinotta, Heavy ion carcinogenesis and human space exploration. *Nature Rev. Cancer* **8**, 465-472 (2008).

4. D.T. Goodhead, Initial events in the cellular effects of ionising radiation: clustered damage in DNA. *Int. J. Radiat. Biol.* **65**, 7-17 (1994).

5. F.A. Cucinotta, H. Nikjoo and D.T. Goodhead, Model of the radial distribution of energy imparted in nanometer volumes from HZE Particles. *Radiat. Res.* **153**, 459-468 (2000).

6. A. Ponomarev, S. Costes and F.A. Cucinotta, Stochastic properties of radiation induced DSB: DSB distributions in large scale chromatin loops, the HPRT gene and within the visible volumes of DNA repair foci. *Int. J. Radiat. Biol.* **84**, 916-929 (2008).

7. S.V. Costes, A. Ponomarev, J.L. Chen, D. Nguyen, F.A. Cucinotta, and M.H. Barcellos-Hoff, Image-based modeling reveals dynamic redistribution of DNA damage into nuclear sub-domains. *PLoS Comp. Biol.* **3**, 1-12 (2007).

8. S.H. MacPhail, J.P. Banath, Y.Yu, E. Chu, and P.L. Olive, Cell cycle-dependent expression of phosphorylated histone H2AX: reduced expression in unirradiated but not X-irradiated G1-phase cells. *Radiat. Res.* **159**, 759-767 (2003).

9. O.D. Perez and G.P. Nolan, Simultaneous measurement of multiple active kinase states using polychromatic flow cytometry. *Nat. Biotechnol*. **20**, 155-162 (2002).

10. M.K. Whalen, S.K. Gurai, H. Zahed-Kargaran and J.M. Pluth, Specific ATM-mediated phosphorylation dependent on radiation quality. *Radiat. Res.* **170**, 353-364 (2008).

11. K.K. Tsai, E.Y. Chuang, J.B. Little and Z. M. Yuan, Cellular mechanisms for low-dose ionizing radiation-induced perturbations of the breast tissue microenvironment. *Cancer Res*. **65**, 6734-6744 (2005).

12. R. Cox and W.K Masson, Mutation and inactivation of cultured mammalian cells exposed to beams of accelerated heavy ions. III. Human diploid fibroblasts. *Int. J. Radiat. Biol. Relat. Stud. Phys. Chem. Med*. **36**(2) 149-160, 1979.

13. D.O. Ferguson, J.M. Sekiguchi, S. Chang, K.M. Frank, Y.Gao, R.A. DePinho, and F.W. Alt, The nonhomologous end-joining pathway of DNA repair is required for genomic instability and the suppression of translocations. *Proc. Natl. Acad. Sci.* USA **97**, 6630-6633 (2000).

14. M. Martin, A. Genesca, L. Lutre, I. Jaco, G.E. Taccioli, J. Egozcue, M.A. Blasco, G. Iliakis, and L. Tusell, Post-replicative joining of DNA double strand breaks

causes genomic instability in DNA-PK_{cs}-deficient mouse embryonic fibroblasts. *Cancer Res.* **65**, 10223-10232 (2005).

15. C.J. Bakkenist, and M.B. Kastan, DNA damage activates ATM through intermolecular autophosphorylation and dimmer dissociation. *Nature* **421**, 499-506, (2003).

16. E.P. Rogakou, D.R. Pilch, A.H. Orr, V.S. Ivanova, and W.M. Bonner, DNA double-strand breaks induce histone H2AX phosphorylation on serine 139. *J. Biol. Chem*. **273**, 5858-5868 (1998).

17. E.P. Rogakou, C. Boon, and W.M. Bonner, Megabase chromatin domains involved in DNA double-strand breaks in vivo. *Curr. Opin. in Gen. and Dev.* **12**, 162-169 (2002).

18. T.T. Paull, E.P. Rogakou, V. Yamazaki, C.U. Kirchgessner, M. Gellert, and W.M. Bonner, A critical role for histone H2AX in recruitment of repair factors to nuclear foci after DNA damage. *Curr Biol*. **10**, 886-895, (2000).

19. O.A. Sedelnikova, E.P. Rogakou, I. G. Panyutin and W.M. Bonner, Quantitative detection of ^{125}IdU-induced DNA double-strand breaks with γH2AX antibody. *Rad. Res.* **158**, 486-492 (2002).

20. K. Rothkamm and M. Lobrich, Evidence of lack of DNA double-strand break repair in human cells exposed to very low X-ray doses. *Proc. Natl. Acad. Sci*. USA **100**, 5057-5062 (2003).

21. S. Y. Fuchs, I. Tappin and Z. Ronai, Stability of the ATF2 transcription factor is regulated by phosphorylation and dephosphorylation. *J. Biol. Chem.* **275**, 12560-12564 (2000).

22. D. L. Crowe and B. Shemirani, The transcription factor ATF-2 inhibits extracellular signal regulated kinase expression and proliferation of human cancer cells. *Anticancer Res.* **20**, 2945-2949 (2000).

23. A. Bhoumik, S. Takahashi, W. Breitweiser, Y. Shiloh, N. Jones and Z. Ronai, ATM-dependent phosphorylation of ATF2 is required for the DNA damage response. *Mol. Cell* **18**, 577-587 (2005).

24. S. T. Kim, B. Xu and M. B. Kastan, Involvement of the cohesin protein, Smc1, in Atm-dependent and independent responses to DNA damage. *Genes Dev.* **16**, 560-570 (2002).

25. R. Kitagawa, C. J. Bakkenist, P. J. McKinnon and M. B. Kastan, Phosphorylation of SMC1 is a critical downstream event in the ATM-NBS1-BRCA1 pathway. *Genes Dev.* **18**, 1423-1438 (2004).

26. S.T. Kim, B. Xu, and M.B. Kastan, Involvement of the cohesin protein, Smc1, in ATM-dependent and independent responses to DNA damage. *Genes Dev.* **16**, 560-570 (2002).

27. J. Fried, Method for the quantitative evaluation of data from flow microfluorometry. *Comps. & Biomed. Res.* **9**, 263-276 (1976).

28. L.T. Eudey, Statistical considerations in DNA flow cytometry. *Statistical Sci.* **11**, 320-334 (1996).

29. Fraley, Chris and Adrian Raftery (2007). MCLUST Version 3 for R: Normal Mixture Modeling and Model-Based Clustering. Technical Report No. 504. Department of Statistics, U of Washington. Fraley, Chris and Adrian Raftery (2008). mclust: Model-Based Clustering / Normal Mixture Modeling. R package version 3.1-5. http://www.stat.washington.edu/fraley/mclust

30. Elandt-Johnson, R.C., and Johnson, N.L. Survival Models and Data Analysis. John Wiley and Sons, New York, 1999.

31. J.O. Friedrich, K.J. Neill, A. Adhikari and J. Beyene, The ratio of means method as an alternative to mean differences for analyzing continuous outcome variables in meta-analysis: A simulation study. *BMC Med. Res. Method.* Doi: 10.1186/1471-2288-8-32 (2008).

32. G. Schwarz, Estimating the dimension of a model. *Ann. Statistics* **6**, 461-464 (1978). G. Schwarz, Meta: Meta-Analysis. R package version 0.8-2 (2007).

33. M. Gulston, J. Fulford, T. Jenner, C. de Lara, and P. O'Neill, Clustered DNA damage induced by γ-radiation in human fibroblasts (HF19), hamster (V79-4) cells and plasmid DNA is revealed as Fpg and Nth sensitive sites. *Nucl. Acids Res*. **30**, 3464-3472 (2002).

34. A. Ponomarev, and F.A. Cucinotta, Chromatin loops are responsible for higher counts of small DNA fragments induced by high-LET radiation, while chromosomal

domains do not affect the fragment sizes. *Int. J. Radiat. Biol.* **82**, 293-305 (2006).

35. N. Desai, E. Davis, P. O'Neill, M. Durante, F.A. Cucinotta, and H. Wu, Immunofluorescent detection of DNA double strand breaks induced by high-LET radiation. *Radiat. Res.* **164**, 518-521 (2005).

36. F.A. Cucinotta, J.M. Pluth, J. Anderson, J.V. Harper, and P. O'Neill, Biochemical kinetics model of DSB repair And γH2AX foci by non-homologous end joining. *Radiat. Res.* **169**, 214-222 (2008).

37. M.D. Rainey, M.E. Charlton, R.V. Stanton, and M.B. Kastan, Transient inhibition of ATM kinase is sufficient to enhance cellular sensitivity to ionizing radiation. *Cancer Res.* **68**(18) 7466-7474 (2008).

38. S.H. MacPhail, J.P. Banath, T.Y. Yu, E.H. Chu, H. Lambur and P.L. Olive, Expression of phosphorylated histone H2AX in cultured cell lines following exposure to X-rays. *Int. J. Radiat. Biol.* **79**(5) 351-358 (2003).

39. J.H. Petrini, and T.H. Stracker, The cellular response to DNA double-strand breaks: defining the sensors and mediators. *Trends Cell Biol.* **13**(9) 458-462 (2003).

40. G.E. Iliakis and R. Okayasu, Radiosensitivity throughout the cell cycle and repair of potentially lethal damage and DNA double-strand breaks in an X-ray-sensitive CHO mutant. *Int. J. Radiat. Biol*. **57**, 1195-1211 (1990).

41. J.P. Freyer, K. Jarrett, S. Carpenter, and M.R. Raju, Oxygen enhancement ratio as a function of dose and cell cycle phase for radiation-resistant and sensitive CHO cells.

Rad. Res., **127**, 297-307 (1991).

42. H. Wang, S. Liu, P. Zhang, S. Zhang, M. Naidu, H. Wang, and Y. Wang, S-phase cells are more sensitive to high-linear energy transfer radiation. *Int. J. Rad. Oncol. Biol. Phys.* **74**, 1236-1241 (2009).

43. T.J. Jenner, M. Belli, D.T. Goodhead, F. Ianzini, G. Simone, and M.A. Tabocchini, Direct comparison of biological effectiveness of protons and alpha particles of the same LET III. Initial Yield of DNA double-strand breaks in V79 cells. *Int J. Radiat. Biol*. **61**, 631-637 (1992).

44. K. M. Prise, Use of radiation quality as a probe for DNA lesion complexity *Int. J. Radiat. Biol.* **65**, 43–48 (1994).

45. B. Rydberg, M. Lobrich and P. K. Cooper, DNA double-strand breaks induced by high-energy neon and iron ions in human fibroblasts. I. Pulsed-field gel electrophoresis method. *Radiat. Res.* **139**, 133–141 (1994).

46. M. Belli, A. Campa, V. Dini, G. Esposito, Y. Furusawa, G. Simone, E. Sorrentini, and M.A. Tabocchini, DNA fragmentation induced in human fibroblasts by accelerated ions of different energies. *Radiat. Res.* **165**, 713-720 (2006).

47. B. Rydberg, Radiation-induced heat-labile sites that convert into DNA double-strand breaks. *Radiat. Res.* **153**, 805-12 (2000).

Table 1. p-Values for KS Test Statistic of phospho-protein expression for irradiated samples over matched controls for combined S-G2-M cell cycle phases. Values listed are from combined experiments calculated using Fischer's exact test (Equation 2).

	X-ray Dose		Fe nuclei Dose	
	0.05 Gy	***0.1 Gy***	***0.05 Gy***	***0.1 Gy***
γH2AX				
0.5 h	<1.E-20*	<1.E-20*	0.0167	0.397
2 h	0.0252	0.302	1.41E-18*	5.51E-08*
4 h	0.0104	0.00958*	0.000285*	2.46E-10*
8 h	0.00347	0.166	5.47E-11*	1.76E-05*
24 h	0.0115	0.0343	<1.E-20*	1.55E.07*
pATF2				
0.5 h	<1.E-20*	<1.E-20*	<1.E-20*	<1.E-20*
2 h	<1.E-20*	<1.E-20*	1.03E-16*	<1.E-20*
4 h	<1.E-20*	2.5E-20*	0.0544	<1.E-20*
8 h	<1.E-20*	<1.E-20*	3.62E-05*	<1.E-20*
24 h	0.0145	<1.E-20*	0.0058	2.19E-07*

*Significant p-value <0.05

Table 2. Kinetic values for phospho-protein decay following irradiation of 82-6 hTERT fibroblasts.

	Mean Values for X-rays				Mean Values for Fe Nuclei			
	G1 Cells		***S/G2 Cells***		***G1 Cells***		***S/G2 Cells***	
γH2AX	**Value**	**Std. Err.**	**Value**	**Std. Err.**	**Value**	**Std. Err.**	**Value**	**Std. Err.**
t_c, h	3.26	0.76	2.87	0.45	4.50	0.46	5.51	2.94
N_1	1.37	0.46	1.00	0.07	2.05	0.12	0.58	0.15
C_1	0.07	0.05	-0.11	0.05	0.35	0.04	-0.16	0.07
pATF2								
t_c, h	9.05	2.51	7.33	4.56	12.62	3.98	15.65	11.05
N_1	3.75	0.45	2.47	0.75	1.97	0.45	1.19	0.15
N_2	-1.24	0.21	-0.93	0.30	-0.84	0.22	-0.40	0.09
C_1	0.16	0.09	0.31	0.05	0.41	0.09	0.22	0.12

Table 3. RBEs for Fe nuclei compared to X-rays at 2-h and 24-h post-irradiation, and for residual levels of γH2AX and pATF2.

γH2AX	***G1***	***S-G2/M***
2 h	2.05 ± 0.61	0.62 ± 0.17
24 h	5.02 ± 3.47	1.46 ± 0.82
Residual	4.94 ± 3.58	NA

pATF2	***G1***	***S-G2/M***
2 h	0.66 ± 0.13	0.58 ± 0.12
24 h	1.66 ± 0.46	1.18 ± 0.58
Residual	2.56 ± 1.56	0.71 ± 0.41

*RBEs for pATF2 are applicable for low dose only using linear dose response terms, while ignoring quadratic dose terms in Eq. (8).

Figure Captions

Figure 1. Schematic diagram depicting how we plan to use modeling to separate γH2AX intensities measured by flow cytometry into separate distributions for cell cycle phase (G1, S and G2-M) and for distributions of background vs. irradiation induced fluorescence intensity. Blue diamond shapes indicate unirradiated cells containing background levels of fluorescence, with major population circled and labeled "control", and red dots indicate fluorescence levels of irradiated cells, with major population circled in red dotted line and labeled "Radiation".

Figure 2. Model predictions for the probability of a cell containing the designated number of double-strand breaks (DSB) following various doses of X-rays and Fe ion exposure. Left panel shows lower doses of 0.05 and 0.1 Gy and right panel shows higher doses of 0.5 and 2 Gy.

Figure 3. Statistical analysis of cell cycle phase specific densities of γH2AX intensity for different doses of X-rays (upper panels) and Fe nuclei (lower panels) at 2 h post irradiation. The density represents the probability of cells having the intensity values shown that results from the numerical approach described in the text.

Figure 4. Statistical analysis of cell cycle phase specific cumulative distribution of γH2AX intensity for different doses of X-rays (upper panels) and Fe ion nuclei (lower panels) at 2 h post irradiation.

Figure 5. Statistical analysis of cell cycle phase specific densities (fraction of cells) of pATF2 intensity for different doses of X-rays (upper panels) and Fe nuclei (lower panels) at 2 h post irradiation. The density represents the probability of cells having the intensity values shown that results from our numerical approach described in the text.

Figure 6. Comparison of the width of the phospho-protein distribution defined as the range of intensity from the 10% to 90% cell distributions for G1 cells for X-rays versus Fe ion, upper panels γH2AX (A), and lower panels pATF2 (B), with Fe ion shown as filled circles and X-ray as open upside down triangle. Timepoints after irradiation are noted above each graph (0.5, 2, 4, and 24 h).

Figure 7. Decay plots for γH2AX (A) following 2 Gy of X-ray as compared to Fe nuclei, and for pATF2 (B). As described in the Methods section each of the 6 symbols at each time point and radiation quality represent one of three independent experiments for early and late G1 in the G1 plots, or S and G2-M in the S-G2-M plots.

Figure 1

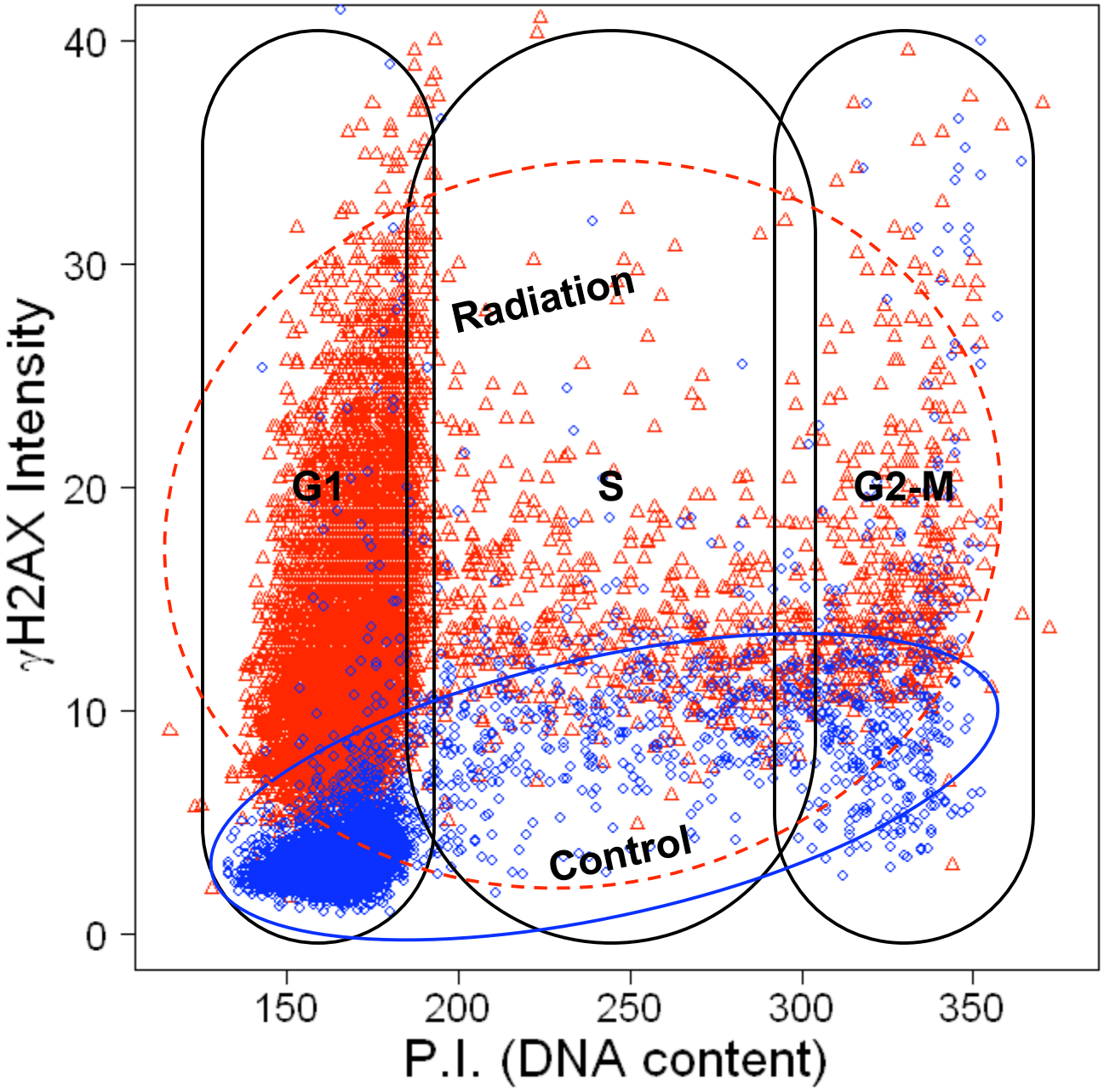
γH2AX Intensity
40
30
20
10
0
150
200
250
300
350
P.I. (DNA content)
Radiation
Control
G1
S
G2-M

Figure 2

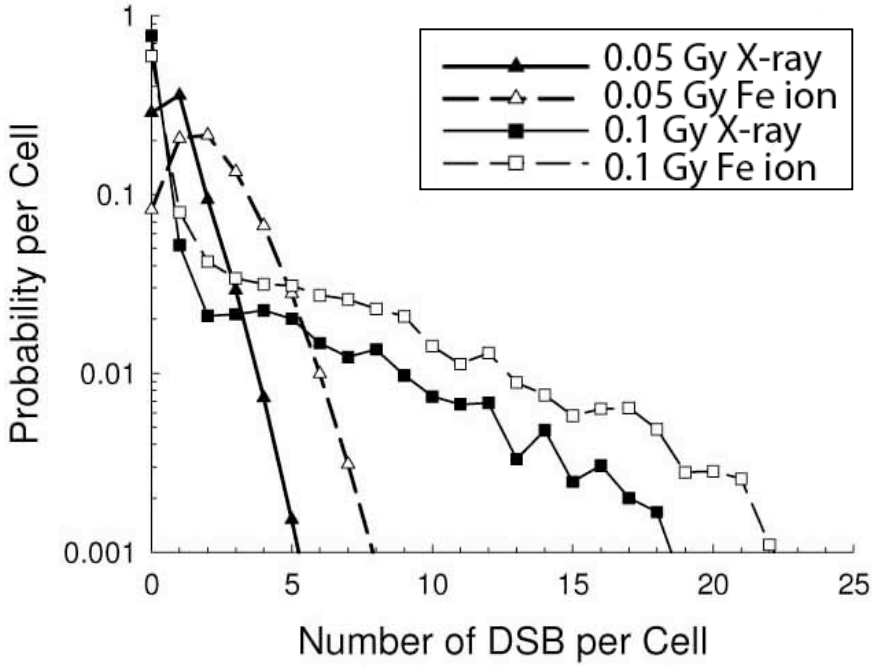
0.05 Gy X-ray
0.05 Gy Fe ion
0.1 Gy X-ray
0.1 Gy Fe ion
Probability per Cell
1
0.1
0.01
0.001
0
5
10
15
20
25
Number of DSB per Cell

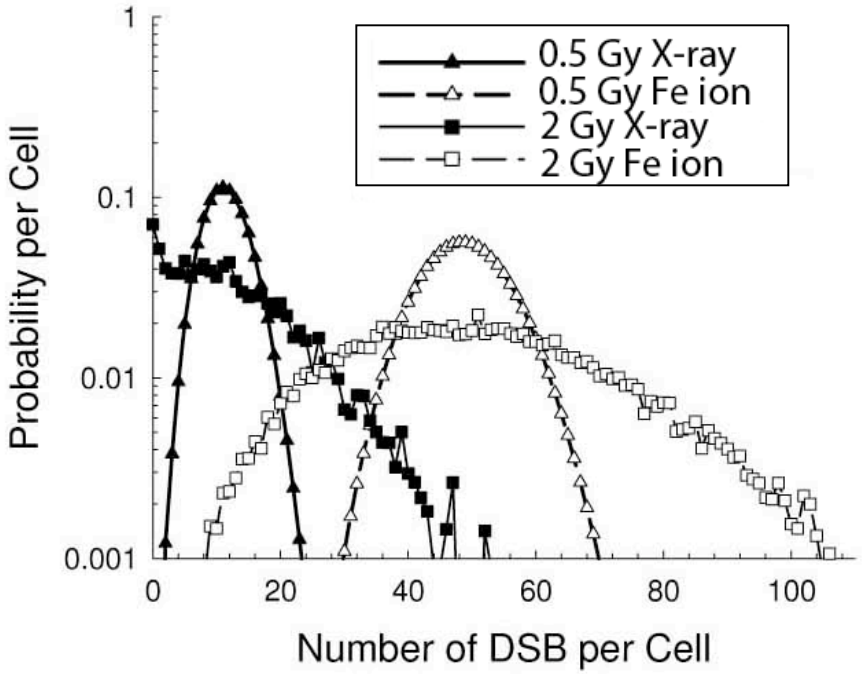
0.5 Gy X-ray
0.5 Gy Fe ion
2 Gy X-ray
2 Gy Fe ion
Probability per Cell
1
0.1
0.01
0.001
0
20
40
60
80
100
Number of DSB per Cell

Figure 3

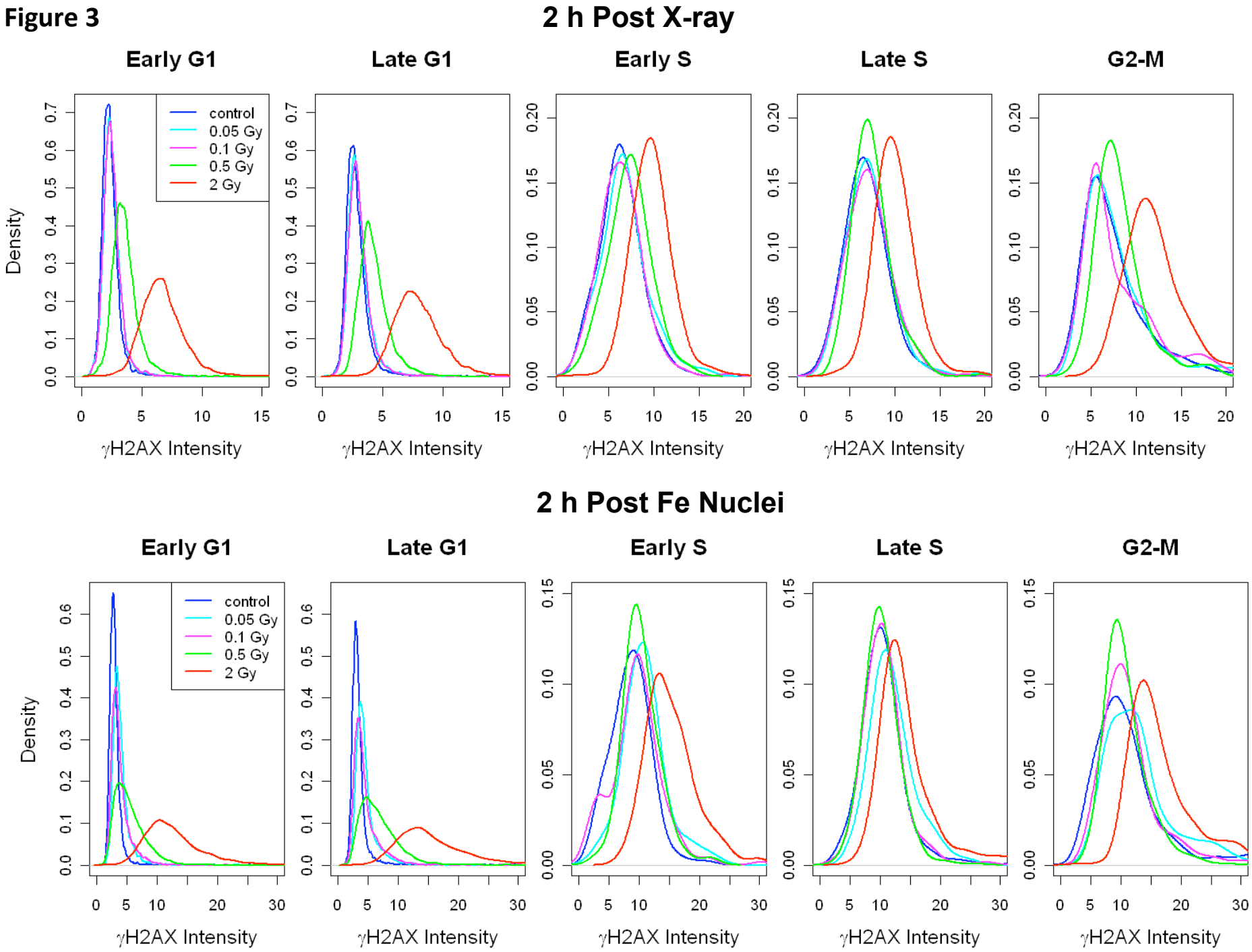
2 h Post X-ray
Early G1
Late G1
Early S
Late S
G2-M
control
0.05 Gy
0.1 Gy
0.5 Gy
2 Gy
Density
γH2AX Intensity
2 h Post Fe Nuclei
Early G1
Late G1
Early S
Late S
G2-M
control
0.05 Gy
0.1 Gy
0.5 Gy
2 Gy
Density
γH2AX Intensity

Figure 4

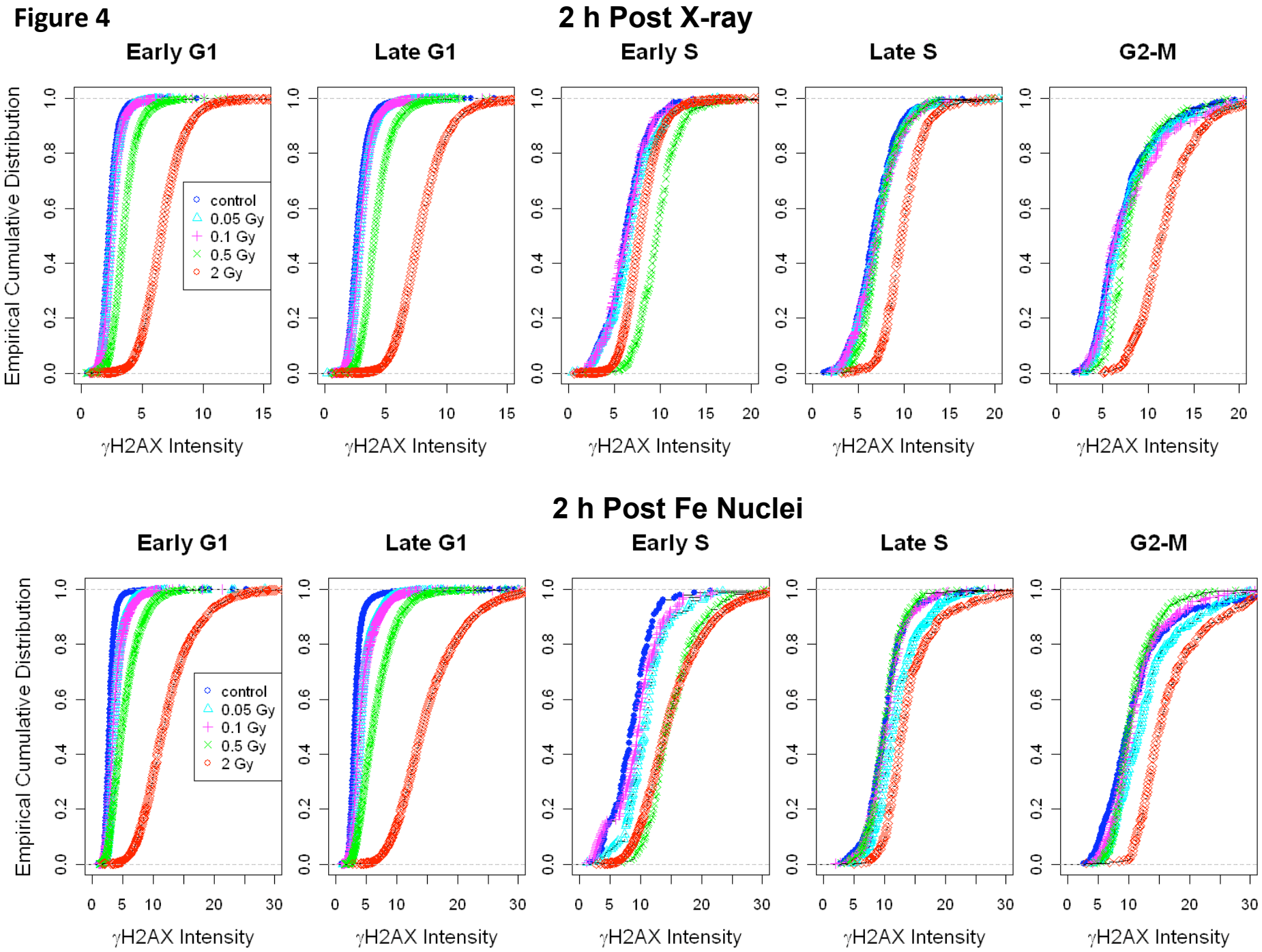
2 h Post X-ray
Early G1
Late G1
Early S
Late S
G2-M
Empirical Cumulative Distribution
control
0.05 Gy
0.1 Gy
0.5 Gy
2 Gy
γH2AX Intensity
2 h Post Fe Nuclei
Early G1
Late G1
Early S
Late S
G2-M
Empirical Cumulative Distribution
control
0.05 Gy
0.1 Gy
0.5 Gy
2 Gy
γH2AX Intensity

Figure 5

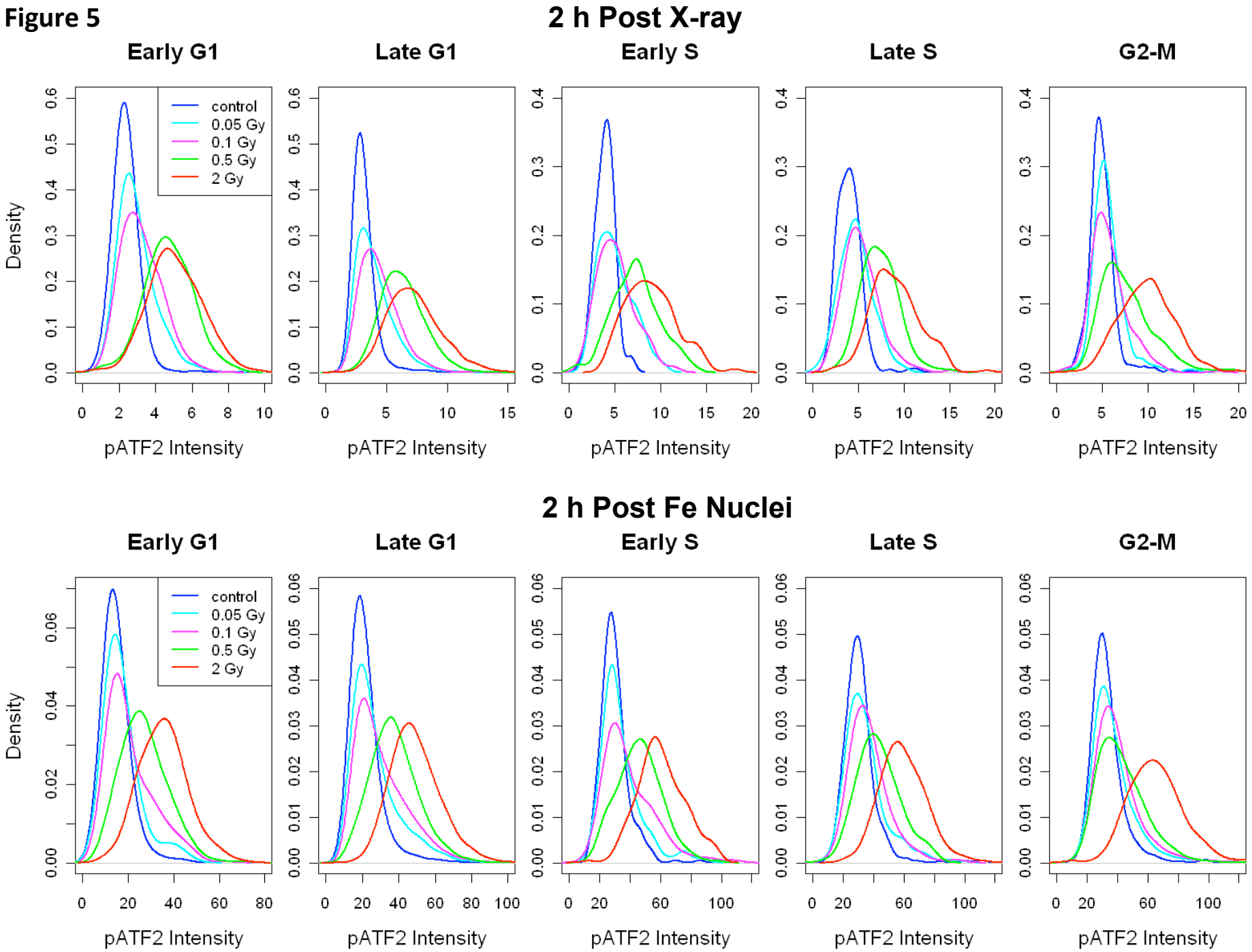
2 h Post X-ray
Early G1
Late G1
Early S
Late S
G2-M
control
0.05 Gy
0.1 Gy
0.5 Gy
2 Gy
Density
pATF2 Intensity
2 h Post Fe Nuclei
Early G1
Late G1
Early S
Late S
G2-M
control
0.05 Gy
0.1 Gy
0.5 Gy
2 Gy
Density
pATF2 Intensity

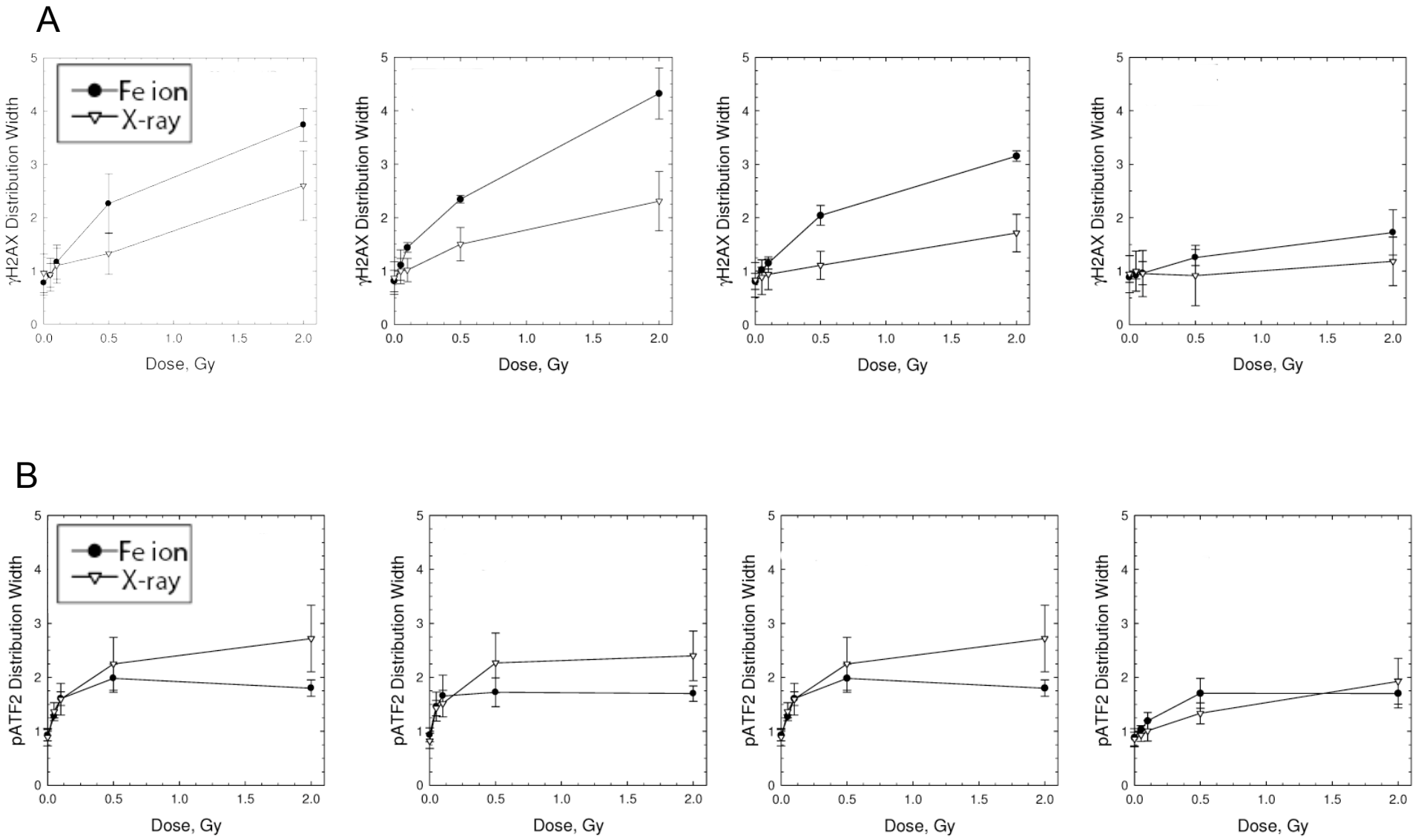
A
Fe ion
X-ray
γH2AX Distribution Width
Dose, Gy
B
Fe ion
X-ray
pATF2 Distribution Width
Dose, Gy

Figure 6

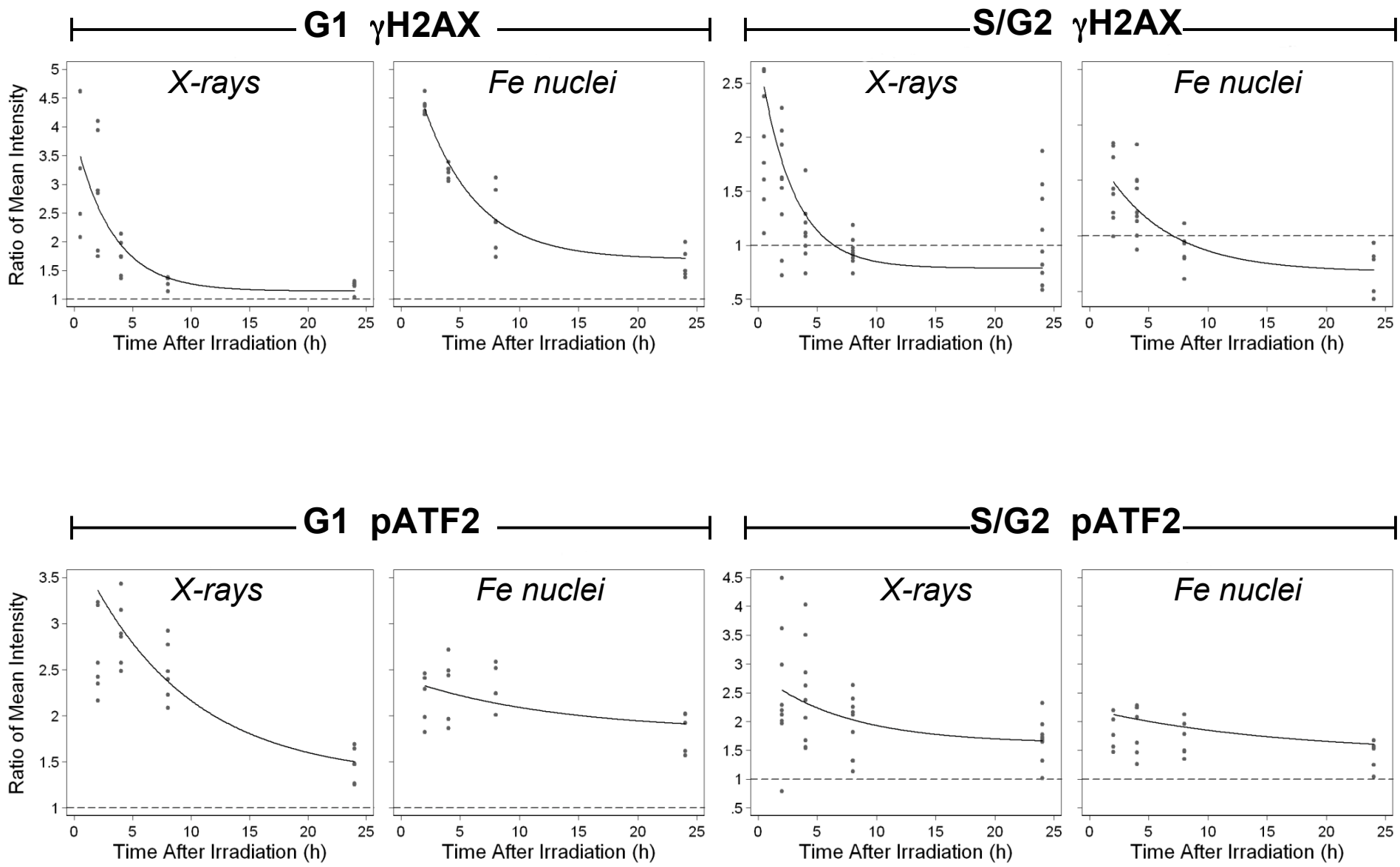
G1 γH2AX
S/G2 γH2AX
G1 pATF2
S/G2 pATF2
X-rays
Fe nuclei
Ratio of Mean Intensity
Time After Irradiation (h)

Figure 7